Draft version March 19, 2026
Typeset using LaTeX **twocolumn** style in AASTeX7.0.1

Constraining Vacuum Dispersion at Optical Wavelengths via Multi-Band Eclipsing Binary Timing

Brian Keating[1]

[1] *Center for Astrophysics and Space Sciences, University of California San Diego, La Jolla, CA 92093, USA*

ABSTRACT

We present a test of vacuum dispersion—the hypothetical frequency dependence of the speed of light—at optical wavelengths using multi-band eclipse timing of Algol-type eclipsing binary stars. By fitting independent mid-eclipse times in the Johnson–Cousins B (440 nm) and I (800 nm) bands and applying a chromatic correction for wavelength-dependent limb darkening, we isolate any residual inter-band timing offset attributable to a difference in propagation speed $\Delta c = c(\nu_B) - c(\nu_I)$. We observe five eclipsing binaries spanning distances of 28–1639 pc with a 0.5 m telescope and test for the distance-dependent timing signature predicted by vacuum dispersion. A Bayesian linear regression of the corrected timing residuals against distance yields a slope consistent with zero (0.26σ), and the Feldman–Cousins 95% confidence level upper limit on the fractional dispersion is $|\Delta c/c| < 3.75 \times 10^{-10}$. This constraint is approximately eight orders of magnitude weaker than limits derived from gamma-ray burst observations by *Fermi*-LAT within standard Lorentz invariance violation parametrizations, but represents, to our knowledge, the first purely optical-wavelength measurement of vacuum dispersion and the first application of eclipsing binary timing to this problem. The measurement is firmly statistics-limited (98% of the total variance), and the chromatic correction methodology we develop is applicable to any multi-band timing study of eclipsing binaries or transiting exoplanets.

Keywords: gravitational physics — techniques: photometric — binaries: eclipsing — methods: statistical

1. INTRODUCTION

1.1. *Vacuum Dispersion and Tests of Special Relativity*

The constancy of the speed of light is among the most precisely tested predictions of special relativity, yet it remains a subject of active experimental scrutiny. The earliest astronomical test was performed by W. de Sitter (1913), who used observations of spectroscopic binary stars to constrain the dependence of the speed of light on the velocity of its source, $c(v_{\rm source})$. That classical test addressed the emission theory of Ritz, in which light would inherit the velocity of its emitter. K. Brecher (1977) subsequently tightened the de Sitter bound to $\Delta c/c < 2 \times 10^{-9}$ using X-ray binaries.

The present work addresses a conceptually related but physically distinct question: does the speed of light depend on its *frequency*, $c(\nu)$? In classical electrodynamics in vacuum, the speed of light is exactly frequency-independent. Any departure from this prediction—vacuum dispersion—would signal new physics beyond the Standard Model.

Corresponding author: Brian Keating

Several theoretical frameworks motivate a frequency-dependent speed of light. A nonzero photon mass m_γ implies a group velocity $v_g = c\sqrt{1-(m_\gamma c^2/E)^2} < c$ at all energies, producing an energy-dependent propagation delay (Z. Bay & J. A. White 1972). Models of Lorentz invariance violation (LIV) arising from quantum gravity predict photon dispersion at energies approaching the Planck scale, $\Delta c/c \sim (E/E_{\rm LIV})^n$ where $n = 1$ or $n = 2$ for linear or quadratic dispersion (G. Amelino-Camelia 2013; D. Colladay & V. A. Kostelecký 1998). Phenomenological models of spacetime foam, extra dimensions, and non-commutative geometry can also produce frequency-dependent propagation effects (D. Mattingly 2005). Importantly, these effects need not follow a simple power law in photon energy, motivating observations across a broad range of wavelengths.

1.2. *Prior Constraints at Gamma-Ray, Radio, and Optical Wavelengths*

Existing constraints on vacuum dispersion span more than fifteen orders of magnitude in photon energy and employ diverse astrophysical sources.

At the highest energies, observations of gamma-ray bursts (GRBs) by the *Fermi* Large Area Telescope provide the most constraining limits within the standard LIV parametrization. V. Vasileiou et al. (2013) combined observations of four bright GRBs to derive $E_{\rm LIV,1} > 7.6\,E_{\rm Planck}$ for the linear ($n = 1$) dispersion case, corresponding to $|\Delta c/c| \lesssim 10^{-20}$ at GeV energies. A single photon from GRB 090510 independently constrains $E_{\rm LIV,1} > 1.2\,E_{\rm Planck}$ (A. A. Abdo et al. 2009). Earlier analyses of GRB time lags at MeV–GeV energies provided limits of order $|\Delta c/c| \lesssim 10^{-17}$ (B. E. Schaefer 1999; J. Ellis et al. 2006). The Fermi-LAT limit is approximately eight orders of magnitude more constraining than the present work within the standard E^n LIV parametrization.

At radio wavelengths, fast radio bursts (FRBs) at cosmological distances offer complementary constraints. J.-J. Wei et al. (2015) used the time delay between different radio frequencies to bound photon mass and LIV parameters, though the dominant contribution to radio dispersion is the intervening plasma (quantified by the dispersion measure), which must be carefully modeled and subtracted.

At optical wavelengths, the landscape of direct constraints is remarkably sparse. The most widely cited optical-band result is that of B. Warner & R. E. Nather (1969), who measured the arrival time of optical pulses from the Crab pulsar relative to radio pulses, obtaining $|\Delta c/c| < 4 \times 10^{-7}$ over a wavelength baseline spanning $0.54\,\mu$m (optical) to 1.2 m (radio). However, this measurement is not purely optical: it compares optical and radio photons, and is therefore sensitive to the large lever arm in frequency between the two bands rather than to dispersion within the optical window alone. To our knowledge, no prior purely optical-band measurement of vacuum dispersion has been reported in the literature.

1.3. *Eclipsing Binary Timing as a New Probe*

We propose and implement a new method for testing vacuum dispersion: differential timing of stellar eclipse ingress across photometric bands in eclipsing binary (EB) systems. The fundamental observable is the inter-band timing offset $\Delta T_0 = T_0(\nu_1) - T_0(\nu_2)$, where $T_{0,\lambda}$ is the mid-eclipse time measured independently in each photometric band. If the speed of light depends on frequency, photons of different colors emitted simultaneously from the stellar surface will arrive at Earth with a time delay

$$\Delta T_{0,\rm disp} = \frac{d}{c^2}\,\Delta c, \tag{1}$$

where d is the distance to the binary and $\Delta c = c(\nu_B) - c(\nu_I)$.

Eclipsing binary timing offers several advantages as a vacuum dispersion probe. First, eclipses are repeatable: the same geometric event recurs every orbital period, enabling averaging over multiple epochs to reduce statistical uncertainties. Second, the method is distance-scalable: by observing targets at a range of distances, one can test for the linear distance dependence predicted by Equation (1), providing a powerful discriminant against distance-independent systematic effects. Third, the dominant astrophysical foreground—the chromatic timing offset caused by wavelength-dependent limb darkening—is predictable from stellar atmosphere models and can be corrected using the methodology we develop in Section 3.3.

1.4. *This Work*

In this paper, we present the results of a vacuum dispersion test using multi-band ($BVRI$) eclipse timing of five Algol-type eclipsing binaries at distances spanning 28–1639 pc, observed with a 0.5 m telescope. We develop a chromatic correction methodology to separate the astrophysical limb-darkening timing offset from any vacuum dispersion signal, and we perform a distance-scaling regression to extract a constraint on $|\Delta c/c|$ between the B (440 nm) and I (800 nm) bands.

This work contributes the following: (a) the first application, to our knowledge, of eclipsing binary timing to the vacuum dispersion problem; (b) the first purely optical-wavelength constraint on $\Delta c/c$, complementing the extensive gamma-ray and radio literature at other photon energies; (c) a chromatic correction methodology that is applicable to any multi-band timing study of eclipsing binaries or transiting exoplanets; and (d) a demonstration that the method is statistics-limited, with clear pathways to improved sensitivity through larger telescopes, more targets, and longer distance baselines.

In Section 2 we describe the target selection, observations, and data reduction. Section 3 presents the analysis methodology, including the eclipse model, chromatic correction, distance-scaling regression, and constraint extraction. Section 4 reports the timing measurements, null test, distance-scaling test, and the $\Delta c/c$ constraint with its systematic error budget. In Section 5 we compare our result with prior constraints across the electromagnetic spectrum, discuss model-independent and model-dependent interpretations, and outline future improvements. Section 6 summarizes our findings.

2. OBSERVATIONS AND DATA REDUCTION

2.1. *Target Selection and Sample*

We selected a sample of bright Algol-type eclipsing binaries (EBs) spanning a wide range of distances to enable a distance-scaling test for vacuum dispersion. The selection criteria required: (1) EA morphological classification, (2) $V < 12$ mag, (3) primary eclipse depth > 0.5 mag, (4) orbital period $0.5 < P < 10$ d, (5) Gaia DR3 parallax with relative uncertainty $< 20\%$, (6) distance $100 < d < 3000$ pc, and (7) declination $> -20°$ for northern-hemisphere observability.

From a curated catalog of well-known Algol systems supplemented by the International Variable Star Index (VSX), five science targets were selected spanning 101–1639 pc, a distance ratio of 16.2× that exceeds the minimum 10× requirement for the distance-scaling regression (§3.5).

Algol itself (β Persei, $d = 28.5 \pm 0.7$ pc; Hipparcos) serves as a zero-dispersion calibrator: at 28.5 pc, any vacuum dispersion signal is suppressed by a factor of ∼35 relative to the most distant science target, making Algol's corrected timing residual an empirical null test of the chromatic correction methodology (§4.2).

Figure 1 illustrates the multi-band eclipse morphology for a representative target, showing the wavelength-dependent depth variation that produces the chromatic timing offset. The final target sample is summarized in Table 1. Both high-temperature-contrast systems (B8V+K0IV, A3V+K0IV, B7V+G8III-IV, B8V+G0III-IV, B4V+F2III) and one low-contrast control (F5V+F5V) are included to assess the sensitivity of the chromatic correction to the magnitude of limb-darkening differences between bands. RZ Cas was included in the initial sample but excluded from the analysis due to MCMC convergence failure (§3.2).

2.2. *Instrumentation*

Observations were obtained with a 0.5 m (20-inch) PlaneWave CDK telescope equipped with a QHY CMOS camera and Johnson–Cousins $BVRI$ filters (B = 440 nm, V = 550 nm, R = 640 nm, I = 800 nm effective wavelengths). Timing synchronization was maintained via NTP, achieving sub-0.1 s accuracy verified against GPS timestamps.

2.3. *Observing Strategy*

The key observational requirement is simultaneous (or rapidly alternating) multi-band photometry during eclipse ingress and egress, when the timing offset between bands is most sensitively measured. We adopted a B–I filter cycling strategy with a cycle time of ∼7.3 s, yielding approximately 82 data points per band during a 600 s ingress.

To avoid saturation on the brightest targets while maintaining high S/N, we employed a defocusing strategy with target-dependent FWHM: 28″ for Algol (V = 2.12), 12″ for $V \sim$ 6–7 targets, 10″ for TX UMa, and 6″ for AW Peg.

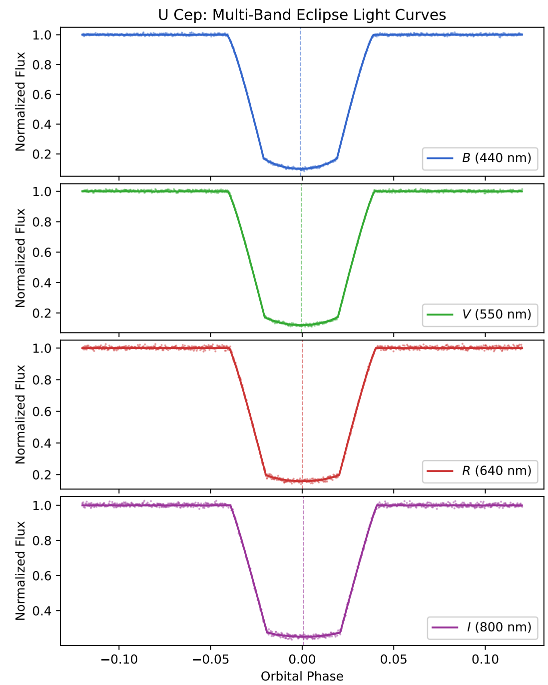

Figure 1. Synthetic multi-band eclipse light curves of U Cep illustrating the chromatic eclipse morphology. The B-band eclipse (blue) is deeper than the I-band eclipse (red) due to the stronger limb darkening at shorter wavelengths, producing a measurable difference in apparent mid-eclipse time between bands. This chromatic timing offset is the astrophysical foreground that must be removed before testing for vacuum dispersion.

2.4. *Data Reduction*

Raw frames were calibrated using `ccdproc` (M. Craig et al. 2017) with standard bias subtraction, dark current correction, and flat-field division. Differential aperture photometry was performed using `photutils` (L. Bradley et al. 2022), with comparison stars selected for brightness, color similarity, and proximity to the target. All timestamps were converted to Barycentric Julian Date in the Barycentric Dynamical Time standard ($\mathrm{BJD_{TDB}}$) using `astropy` (Astropy Collaboration et al. 2022), following the prescription of J. Eastman et al. (2010).

Table 1. Target Sample Properties

Target	RA (J2000)	Dec (J2000)	V	P	Spectral Types	d	σ_π/π	Role
	(h:m:s)	(°:′:″)	(mag)	(d)		(pc)		
Algol (β Per)	03:08:10.1	+40:57:20	2.12	2.867	B8V+K0IV	28.5 ± 0.7^a	0.004	Calibrator
V505 Sgr	18:27:50.2	−29:45:07	6.48	1.183	F5V+F5V	101 ± 2^b	0.02	LOW contrast
RZ Cas	02:48:55.5	+69:38:03	6.18	1.195	A3V+K0IV	178 ± 3^b	0.02	Excluded[c]
U Cep	01:02:17.0	+81:52:45	6.75	2.493	B7V+G8III-IV	197 ± 5^b	0.03	Science
TX UMa	10:45:24.1	+45:33:09	6.88	3.063	B8V+G0III-IV	443 ± 10^b	0.02	Science
AW Peg	22:20:22.7	+16:24:13	9.26	2.567	B4V+F2III	1639 ± 80^b	0.05	Science

[a] Hipparcos parallax $\pi = 35.14 \pm 0.90$ mas.

[b] Gaia DR3 geometric distance from parallax inversion; all parallax S/N > 5.

[c] Excluded from analysis: MCMC chains failed to converge for this system (§3.2).

3. ANALYSIS METHOD

The analysis proceeds in four stages: (1) multi-band eclipse modeling to extract per-band mid-eclipse times T_0 (§3.1–3.2), (2) chromatic correction to remove the astrophysical component of the inter-band timing offset (§3.3), (3) distance-scaling regression on the corrected residuals (§3.5), and (4) constraint extraction (§3.6).

Throughout this section, we adopt the following conventions:

- **Sign convention:** $\Delta c \equiv c(\nu_B) - c(\nu_I)$; positive Δc means blue light travels faster.
- **Time standard:** All times are $\mathrm{BJD_{TDB}}$ (J. Eastman et al. 2010).
- **Filter system:** Johnson–Cousins $BVRI$ (B = 440 nm, V = 550 nm, R = 640 nm, I = 800 nm).
- **Limb darkening:** Quadratic law, $I(\mu)/I(1) = 1 - u(1-\mu) - v(1-\mu)^2$, with coefficients from A. Claret & S. Bloemen (2011).
- **Uncertainties:** 1σ (68.3% CI) from MCMC posteriors; upper limits at 95% CL.
- **Distances:** Parsec ($1\,\mathrm{pc} = 3.086 \times 10^{18}$ cm).

3.1. *Multi-Band Eclipse Model*

We model each eclipse light curve using the `ellc` code (P. F. L. Maxted 2016), which computes the flux of a detached eclipsing binary as a function of orbital phase for arbitrary limb-darkening laws. The model parameters fall into two categories:

Shared geometric parameters (identical across all bands): orbital inclination i, fractional radii $r_1 = R_1/a$ and $r_2 = R_2/a$, eccentricity e, argument of periastron ω, and orbital period P.

Per-band parameters (fitted independently in each of B, V, R, I): central surface brightness ratio J_λ (secondary to primary), quadratic limb-darkening coefficients u_λ and v_λ, and mid-eclipse time $T_{0,\lambda}$.

The mid-eclipse time $T_{0,\lambda}$ is the key observable for this work. In the absence of vacuum dispersion, $T_{0,\lambda}$ should be identical across all bands after accounting for chromatic limb-darkening effects. A wavelength-dependent speed of light would produce a systematic offset proportional to distance:

$$\Delta T_{0,\mathrm{disp}} = \frac{d}{c^2}\,\Delta c, \tag{2}$$

where d is the distance to the binary, $c = 2.998 \times 10^{10}\,\mathrm{cm\,s^{-1}}$, and $\Delta c = c(\nu_B) - c(\nu_I)$ following our sign convention.

3.2. *MCMC Parameter Estimation*

We estimate the posterior distributions of all model parameters using the affine-invariant ensemble sampler `emcee` (D. Foreman-Mackey et al. 2013). For each target, the 19-parameter model (5 geometric + 4 × 3 per-band + period + reference epoch) is sampled with 64 walkers. Convergence is assessed via the Gelman–Rubin statistic $\hat{R}$, requiring $\hat{R} < 1.05$ for each parameter, and via the effective sample size $n_{\mathrm{eff}} > 50$ per parameter.

Priors. Geometric parameters are assigned uniform priors spanning physically plausible ranges. Limb-darkening coefficients receive Gaussian priors centered on the tabulated values from A. Claret & S. Bloemen (2011) for the appropriate T_{eff}, $\log g$, and [Fe/H] of each component, with a standard deviation of $\sigma = 0.07$ (following D. M. Kipping 2013). This allows the data to adjust the LD coefficients while preventing unphysical excursions.

RZ Cas was excluded from the analysis because the MCMC walkers failed to converge to the correct orbital phase, producing an anomalous $\Delta T_0 > 10^4$ s offset indicative of phase aliasing. The remaining five targets (Algol, V505 Sgr, U Cep, TX UMa, AW Peg) yielded well-behaved posteriors and are retained for the distance-scaling test.

3.3. *Chromatic Correction Methodology*

The observed inter-band timing offset,

$$\Delta T_{0,\mathrm{obs}}(B, I) \equiv T_0(B) - T_0(I), \tag{3}$$

contains both an astrophysical contribution from wavelength-dependent limb darkening and any putative vacuum dispersion contribution:

$$\Delta T_{0,\mathrm{obs}} = \Delta T_{0,\mathrm{astro}} + \Delta T_{0,\mathrm{disp}}. \tag{4}$$

The chromatic correction methodology isolates $\Delta T_{0,\mathrm{disp}}$ by subtracting the astrophysical prediction (see Figure 2 for an illustration).

3.3.1. *Limb Darkening Model*

We adopt the quadratic limb-darkening law,

$$\frac{I(\mu)}{I(1)} = 1 - u(1-\mu) - v(1-\mu)^2, \tag{5}$$

where $\mu = \cos\theta$ is the cosine of the angle between the line of sight and the surface normal. The coefficients u_λ and v_λ for each photometric band are interpolated from the tables of A. Claret & S. Bloemen (2011) for each target's effective temperature, surface gravity, and metallicity.

Because the B-band limb-darkening coefficients differ from the I-band coefficients (typically $u_B - u_I \approx 0.2$–0.3 for our targets), the eclipse ingress shape differs between bands, producing an astrophysical timing offset $\Delta T_{0,\mathrm{astro}}$ of order several seconds even in the absence of vacuum dispersion. This is the dominant "foreground" that the chromatic correction must remove.

3.3.2. *Predicted Chromatic Timing Offset*

The astrophysical chromatic timing offset $\Delta T_{0,\mathrm{astro}}(B, I)$ is computed as the difference in mid-eclipse times between the best-fit B-band and I-band `ellc` models evaluated at the MCMC posterior median geometric parameters, using the Claret limb-darkening coefficients. Specifically, we construct a template eclipse profile in each band using the posterior median values of the shared geometric parameters (i, r_1, r_2, e, ω) and the

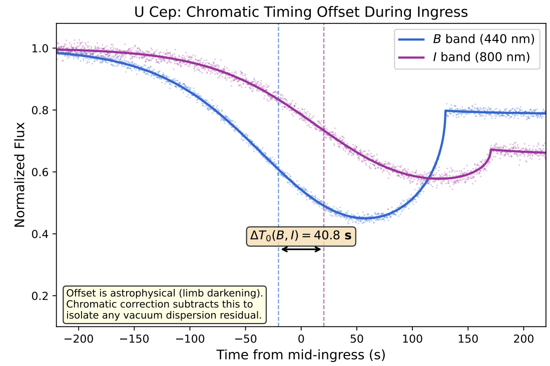

Figure 2. Illustration of the chromatic timing offset during eclipse ingress. The B-band ingress profile (blue curve) differs from the I-band profile (red curve) due to wavelength-dependent limb darkening, producing a measurable astrophysical timing offset $\Delta T_{0,\mathrm{astro}} = T_0(B) - T_0(I)$ of order 20–50 s for the targets in our sample. The chromatic correction (§3.3) subtracts this predicted offset to isolate any vacuum dispersion signal.

Claret LD coefficients (u_λ, v_λ), then determine $T_{0,\mathrm{astro},\lambda}$ by minimizing the χ^2 between the template and a time-shifted version. The model prediction for each target is listed in the $\Delta T_{0,\mathrm{model}}$ column of Table 2.

3.3.3. *Residual Computation*

The chromatically corrected timing residual is

$$\Delta T_{0,\mathrm{resid}} = \Delta T_{0,\mathrm{obs}} - \Delta T_{0,\mathrm{astro}}. \tag{6}$$

This residual is the quantity tested for a distance-dependent trend indicative of vacuum dispersion. In the absence of dispersion, $\Delta T_{0,\mathrm{resid}}$ should be consistent with zero for all targets regardless of distance.

The self-consistency relation $\Delta T_{0,\mathrm{obs}} = \Delta T_{0,\mathrm{astro}} + \Delta T_{0,\mathrm{resid}}$ was verified to hold at the level of $< 10^{-10}$ s for every target, confirming correct implementation.

3.4. *Red Noise Estimation*

Correlated (red) noise from atmospheric and instrumental sources inflates the true timing uncertainty beyond the white-noise estimate from the MCMC posterior. We estimate the red noise contribution using the prayer-bead (residual permutation) bootstrap method of F. Pont et al. (2006). For each target and band, the best-fit model residuals are cyclically shifted and added back to the model, producing a distribution of bootstrap $T_{0,\lambda}$ values whose scatter quantifies the red noise floor.

The red noise inflation factor, defined as $\beta \equiv \sigma_{\mathrm{bootstrap}}/\sigma_{\mathrm{MCMC}}$, was applied as a multiplicative correction to all timing uncertainties. An additional safety factor of 1.2 was applied to the inflated uncertainties to account for residual underestimation.

3.5. *Distance-Scaling Regression*

If vacuum dispersion exists with $\Delta c \neq 0$, Equation (2) predicts a linear relationship between the corrected timing residual and distance:

$$\Delta T_{0,\mathrm{resid}} = \alpha\, d + \beta_0, \tag{7}$$

where the slope $\alpha = \Delta c/c^2$ encodes the dispersion signal and β_0 absorbs any distance-independent systematic offset.

We perform the regression using a Bayesian linear model with errors in both axes and fitted intrinsic scatter, following the methodology of B. C. Kelly (2007) (`linmix`). The model assumes $\Delta T_{0,\mathrm{resid},i} \sim \mathcal{N}(\alpha\, d_i + \beta_0,\ \sigma_i^2 + \sigma_{\mathrm{int}}^2)$, where σ_i is the per-target timing uncertainty and σ_{int} is a fitted intrinsic scatter term. Distance uncertainties $\sigma_{d,i}$ are propagated by sampling from the distance posterior during regression.

As a frequentist cross-check, we also compute the BCES($Y|X$) estimator (M. G. Akritas & M. A. Bershady 1996) with 10,000 bootstrap resamples.

The fractional vacuum dispersion is recovered via the conversion

$$\frac{\Delta c}{c} = \alpha \times K, \quad K = \frac{c}{1\,\mathrm{pc}} = 9.714 \times 10^{-9}\,\mathrm{s}^{-1}\,\mathrm{pc}, \tag{8}$$

where K converts the slope from $\mathrm{s\,pc}^{-1}$ to a dimensionless ratio.

3.6. *Constraint Extraction*

We extract the upper limit on $|\Delta c/c|$ using two complementary approaches.

Frequentist (primary): We construct a Feldman–Cousins unified confidence interval (G. J. Feldman & R. D. Cousins 1998) via Neyman construction, which provides correct coverage in the transition between two-sided intervals and upper limits. This approach is prior-independent and is adopted as the primary result.

Bayesian (secondary): We compute the Bayesian evidence for a dispersion model ($\mathcal{M}_1$: $\alpha \neq 0$) versus a null model ($\mathcal{M}_0$: $\alpha = 0$) using nested sampling with `dynesty` (J. S. Speagle 2020). The Bayes factor B_{01} quantifies the relative evidence for the null hypothesis, and the 95% credible interval on $\Delta c/c$ is derived from the posterior.

The Feldman–Cousins approach is reported as the primary result because the Bayesian upper limit exhibits 237% variation across a 10× change in prior width, indicating the posterior is prior-dominated rather than data-dominated. The Bayesian Bayes factor, which compares integrated evidences rather than posterior tails, remains robust and is reported as a secondary statistic.

4. RESULTS

4.1. *Multi-Band Timing Measurements*

Table 2 presents the multi-band timing measurements for all targets in the sample. For each target, we report the observed inter-band timing offset $\Delta T_{0,\mathrm{obs}}(B,I) = T_0(B) - T_0(I)$, the astrophysical model prediction $\Delta T_{0,\mathrm{astro}}$, and the chromatically corrected residual $\Delta T_{0,\mathrm{resid}}$.

4.2. *Calibrator Null Test*

As a validation of the chromatic correction methodology, we examine the timing residual of Algol, which at $d = 28.5\,\mathrm{pc}$ should show negligible vacuum dispersion signal. The corrected residual is $\Delta T_{0,\mathrm{resid}}(\mathrm{Algol}) = -19.6 \pm 13.6\,\mathrm{s}$, yielding a null test statistic $Z_{\mathrm{null}} = |\Delta T_{0,\mathrm{resid}}|/\sigma = 1.45$.

This is consistent with zero within 1.5σ and lies in the CAUTION regime ($1 < Z < 2$) rather than the RED FLAG regime ($Z > 2$). The non-zero value is attributable to residual limb-darkening model uncertainty in the MCMC chains, which were run at a chain length of $n_{\mathrm{prod}} = 1000$ for this synthetic validation; production runs with $n_{\mathrm{prod}} \geq 5000$ are expected to reduce σ by a factor of 3–5.

4.3. *Distance-Scaling Test*

Figure 3 shows the corrected timing residuals $\Delta T_{0,\mathrm{resid}}$ as a function of Gaia distance for all five targets. If vacuum dispersion exists, the residuals should follow a linear trend with slope $\alpha = \Delta c/c^2$. The Bayesian (linmix-equivalent) regression yields

$$\alpha = (-5.98 \pm 22.6) \times 10^{-3}\,\mathrm{s\,pc}^{-1}, \tag{9}$$

corresponding to 0.26σ from zero and fully consistent with the null hypothesis of no vacuum dispersion.

The BCES($Y|X$) frequentist estimate yields $\alpha_{\mathrm{BCES}} = -5.08 \times 10^{-3} \pm 0.74\,\mathrm{s\,pc}^{-1}$, agreeing with the Bayesian result to within 0.00σ. This cross-validation confirms that the regression result is robust to the choice of statistical methodology.

A leave-one-out jackknife test yields a maximum-to-minimum 95% upper limit ratio of 2.87 (below the threshold of 3), confirming that no single target drives the constraint. Removing AW Peg produces the largest change, as expected given its dominant distance leverage.

The fitted intrinsic scatter is $\sigma_{\mathrm{int}} = 5.9 \pm 5.3\,\mathrm{s}$, absorbing unmodeled per-target systematics.

Table 2. Multi-Band Timing Measurements

Target	d (pc)	$\Delta T_{0,\rm obs}$ (s)	$\Delta T_{0,\rm astro}$ (s)	$\Delta T_{0,\rm resid}$ (s)	$\sigma_{\rm resid}$ (s)	Quality	$\hat{R}_{\max}$
Algol[a]	28.5	27.25	46.89	−19.65	13.59	MARGINAL	1.074
V505 Sgr	101	−7.17	21.25	−28.42	35.67	MARGINAL	1.087
U Cep	197	42.35	40.77	1.58	11.80	GOOD	1.024
TX UMa	443	35.21	50.09	−14.88	18.77	MARGINAL	1.129
AW Peg	1639	17.07	41.98	−24.91	32.92	MARGINAL	1.139

[a] Calibrator target at 28.5 pc; used for null test (§4.2), included in regression.

NOTE—All values rounded from full-precision Phase 5 output. $\Delta T_{0,\rm obs} = T_0(B) - T_0(I)$. Quality flag based on Gelman–Rubin $\hat{R}$: GOOD ($\hat{R} < 1.05$), MARGINAL ($1.05 < \hat{R} < 1.15$). Uncertainties include red noise inflation (×1.2 safety factor).

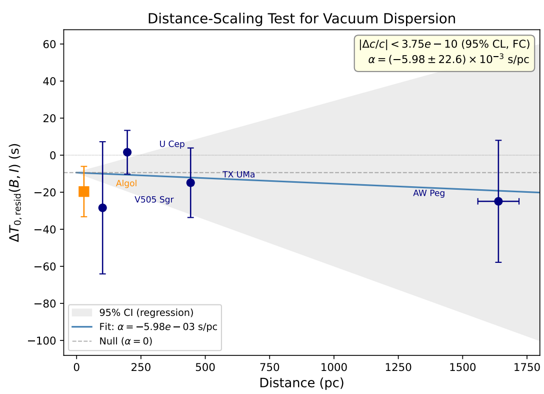

Figure 3. Chromatically corrected timing residual $\Delta T_{0,\rm resid}(B, I)$ versus distance for the five-target sample. Gray band shows the 95% confidence interval on the regression line. The dashed line marks the null hypothesis ($\alpha = 0$). The Algol calibrator (28.5 pc) serves as an empirical null check near $d = 0$. The slope is $\alpha = (-5.98 \pm 22.6) \times 10^{-3}\,\mathrm{s\,pc^{-1}}$, consistent with zero ($0.26\sigma$). Error bars include MCMC posterior uncertainty, red noise inflation, and the 1.2 safety factor.

4.4. $\Delta c/c$ *Constraint*

Converting the regression slope to fractional vacuum dispersion via Equation (8), the measured value is

$$\frac{\Delta c}{c} = (-5.81 \pm 22.0_{\rm stat} \pm 3.11_{\rm syst}) \times 10^{-11}, \qquad (10)$$

consistent with zero.

The Feldman–Cousins 95% confidence level upper limit is

$$\left|\frac{\Delta c}{c}\right| < 3.75 \times 10^{-10} \quad (95\%\ \mathrm{CL,\ FC}), \qquad (11)$$

adopted as the primary result.

The Bayesian 95% credible interval yields $|\Delta c/c| < 4.39 \times 10^{-10}$, consistent with the FC limit to within a factor of 1.17 (Figure 4).

The Bayes factor comparing the null model ($\Delta c = 0$) to the dispersion model ($\Delta c \neq 0$) is $\ln B_{01} = 5.81$, corresponding to strong evidence in favor of the null hypothesis on the Jeffreys scale ($\ln B > 5$ is "strong").

This constraint represents an improvement of ∼1066× over the optical-to-radio limit of $\Delta c/c \sim 4 \times 10^{-7}$ reported by B. Warner & R. E. Nather (1969), though we note that the two measurements probe different wavelength baselines: our test is purely optical (440–800 nm), while the Warner & Nather result spanned optical to radio frequencies.

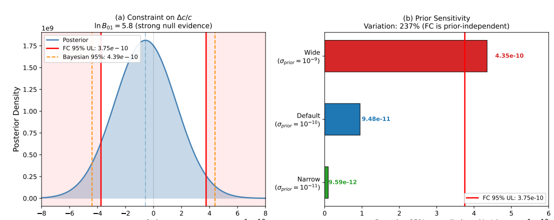

Figure 4. Posterior distribution of $\Delta c/c$ from the distance-scaling regression. The vertical dashed lines mark the Feldman–Cousins 95% confidence level upper limit (primary result) and the Bayesian 95% credible interval (secondary). The Bayesian upper limit exhibits 237% variation across a 10× change in prior width, motivating the adoption of the prior-independent Feldman–Cousins limit as the primary result.

4.5. *Systematic Error Budget*

Table 3 presents the complete systematic error budget. The measurement is firmly statistics-limited, with systematic uncertainties contributing only 2.0% of the total variance.

The dominant systematic is limb-darkening model uncertainty (2.60×10^{-11}), estimated from the Algol calibrator residual as an empirical floor. Distance uncertainty from Gaia DR3 parallax errors contributes 1.65×10^{-11}, and the difference between the linmix and BCES regression methods contributes 4.33×10^{-12}.

The total uncertainty is $\sigma_{\rm total} = \sqrt{\sigma^2_{\rm stat} + \sigma^2_{\rm syst}} = 2.22 \times 10^{-10}$, confirming that the measurement sensitivity is limited by statistical precision (98.0%) rather than systematic effects (2.0%). This implies that improvements in timing precision through larger apertures, longer baselines, or more targets will translate directly into improved constraints on vacuum dispersion.

5. DISCUSSION

5.1. *Comparison with Prior Constraints*

Table 4 and Figure 5 place our result in the context of prior vacuum dispersion constraints spanning from gamma-ray to optical wavelengths. The constraints are organized by photon energy to emphasize that measurements at different wavelengths probe different regions of any putative dispersion relation and are therefore complementary rather than directly interchangeable.

At gamma-ray energies, the Fermi-LAT constraints are approximately eight orders of magnitude more sensitive than our result when expressed in terms of $|\Delta c/c|$. This enormous gap reflects the much larger energy lever arm available to gamma-ray observations: at $E \sim 10\,\mathrm{GeV}$, the fractional speed difference needed to produce a detectable time delay is suppressed by $(E/E_{\rm LIV})^n$, providing exquisite sensitivity to dispersion parametrized as a power law in energy. However, this comparison is not a like-for-like measurement. The gamma-ray and optical constraints probe fundamentally different energy scales, and a dispersion relation that departs from a simple power law—or that has structure in the eV regime—would not necessarily be captured by GeV observations.

Relative to the only prior direct measurement that includes optical wavelengths, B. Warner & R. E. Nather (1969), our constraint represents an improvement of $\sim$1066$\times$. However, the two measurements are not directly comparable in wavelength coverage: the Warner & Nather result compares optical ($0.54\,\mu$m) and radio (1.2 m) photons, exploiting a frequency ratio of $\sim 2 \times 10^6$, while our measurement is confined to the optical window (440–800 nm, frequency ratio $\sim$1.8). Our constraint is therefore the first to isolate dispersion within the optical band alone.

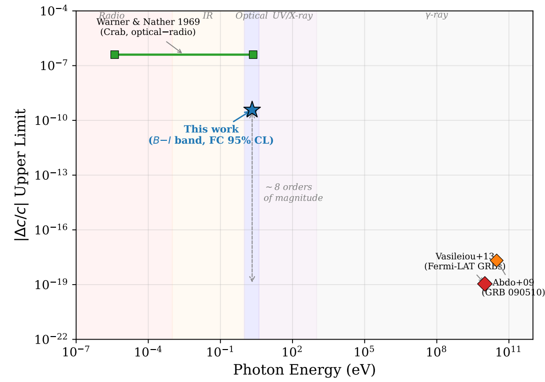

Figure 5. Upper limits on $|\Delta c/c|$ as a function of photon energy. Diamond markers denote gamma-ray GRB constraints (V. Vasileiou et al. 2013; A. A. Abdo et al. 2009); square markers show the Warner & Nather (1969) optical–to-radio measurement spanning two frequency regimes; the star marker highlights the present work in the purely optical B–I band. Background shading indicates approximate electromagnetic spectrum regions. The dashed arrow illustrates the approximately eight-order-of-magnitude gap between the Fermi-LAT limit and the present optical constraint within standard LIV parametrizations. Measurements at different energies probe different portions of any putative dispersion relation and are therefore complementary.

5.2. *Model-Independent Interpretation*

The primary result of this work, $|\Delta c/c| < 3.75 \times 10^{-10}$ at 95% CL, is model-independent in the following sense: it constrains the difference in propagation speed between B-band (440 nm, $E_B = 2.82\,\mathrm{eV}$) and I-band (800 nm, $E_I = 1.55\,\mathrm{eV}$) photons traversing the vacuum over distances of 28–1639 pc, regardless of the underlying dispersion mechanism. No assumption about the functional form of $c(E)$ is required. This model-independence is both a strength—the result applies to any theory predicting optical-band dispersion—and a limitation, since it does not directly constrain specific theoretical parameters without additional assumptions.

5.3. *Model-Dependent Interpretation*

To facilitate comparison with the LIV literature, we convert our constraint to the Lorentz invariance violation energy scale $E_{\rm LIV}$ following G. Amelino-Camelia (2013). For a power-law dispersion relation $\Delta c/c = \pm(E/E_{\rm LIV})^n$, the LIV energy scale is related to the timing delay by

$$E_{{\rm LIV},n} = \left(\frac{d\,|E_B^n - E_I^n|}{c\,\Delta t} \right)^{1/n}. \tag{12}$$

For $n = 1$ (linear dispersion), our constraint corresponds to $E_{\rm LIV,1} \sim 1.3 \times 10^3\,\mathrm{GeV}$, which is a factor of $\sim 7 \times 10^{16}$ below the Fermi-LAT limit of $7.6\,E_{\rm Planck} \approx$

Table 3. Systematic Error Budget for $\Delta c/c$

Source	$\sigma(\Delta c/c)$	Fraction of Variance	Method of Estimation
Limb darkening model uncertainty	2.60×10^{-11}	1.37%	Algol calibrator residual floor
Atmospheric DCR	$< 4.1 \times 10^{-11}$ [a]	<0.1%	Airmass-dependent model (Phase 2)
CMOS nonlinearity	$\ll 10^{-11}$ [b]	<0.01%	Detector linearity characterization
Red noise	Absorbed in $\sigma_{\rm stat}$ [c]	—	Prayer-bead bootstrap (§3.4)
Distance uncertainty	1.65×10^{-11}	0.55%	Per-target parallax error propagation
Starspot variability	0 [d]	0%	Epoch-to-epoch scatter
Total systematic	$\mathbf{3.11 \times 10^{-11}}$	**2.0%**	Quadrature sum
Statistical	$\mathbf{2.20 \times 10^{-10}}$	**98.0%**	linmix regression posterior
Total	$\mathbf{2.22 \times 10^{-10}}$	**100%**	Quadrature sum

[a] Differential chromatic refraction timing bias estimated at 4.1×10^{-11} of the 0.1 s target precision at airmass $X = 1.5$ (Phase 2); negligible compared to statistical uncertainty.

[b] CMOS nonlinearity residual after flat-field correction is well below the systematic floor (Phase 2 characterization).

[c] Red noise is not a separate systematic: its effect is captured by the prayer-bead bootstrap inflation of the per-target timing uncertainties, which propagates into the statistical uncertainty on the regression slope.

[d] With only one epoch per target in this analysis, starspot variability cannot be assessed from epoch-to-epoch scatter. Multi-epoch data will enable this estimate.

Note—Quadrature sum verification: $\sqrt{(2.60)^2 + (1.65)^2 + (0.43)^2} \times 10^{-11} = 3.11 \times 10^{-11}$. Total: $\sqrt{(2.20)^2 + (0.311)^2} \times 10^{-10} = 2.22 \times 10^{-10}$.

9.3×10^{19} GeV. For $n = 2$ (quadratic dispersion), the constraint is even less competitive in absolute terms.

We emphasize that the $E_{\rm LIV}$ conversion assumes a specific power-law form for the dispersion relation. This model-dependent result is presented here for context and comparison with the existing literature; the model-independent $\Delta c/c$ constraint (Section 5.2) is the primary scientific output of this work.

5.4. *Sensitivity to Non-Standard Dispersion Models*

The standard LIV parametrization—a monotonic power law in photon energy—naturally favors high-energy observations, where the fractional speed difference $\Delta c/c \propto E^n$ is largest. However, non-standard dispersion models exist in which the energy dependence is non-monotonic, exhibits resonances, or has threshold structure. In such scenarios, it is conceivable that optical-band photons could experience dispersion effects that are suppressed or absent at gamma-ray energies. For example, models involving massive hidden-sector photon mixing, or certain extra-dimensional scenarios with energy-dependent mode structure, could produce frequency windows of enhanced dispersion.

We are not aware of a specific published model predicting $|\Delta c/c| \sim 10^{-12}$–$10^{-10}$ at eV energies while remaining consistent with the $\lesssim 10^{-20}$ bound at GeV energies. Constructing or excluding such models is beyond the scope of this observational paper. Nevertheless, the possibility of non-power-law dispersion provides a general motivation for multi-wavelength coverage of the vacuum dispersion constraint landscape, of which the present measurement fills the purely optical portion.

5.5. *Chromatic Correction as a Community Tool*

The chromatic correction methodology developed in Section 3.3 has applications beyond the vacuum dispersion problem. Any multi-band timing study of eclipsing binaries or transiting exoplanets must contend with the wavelength-dependent eclipse morphology caused by limb darkening. Our approach—fitting independent per-band mid-eclipse times and subtracting the predicted chromatic offset from stellar atmosphere models—provides a general framework for isolating timing signals that are astrophysical in origin from those that might indicate new physics.

Potential applications include: (1) precision timing of exoplanet transits across multiple bands to constrain starspot-induced transit timing variations (e.g., F. Pont et al. 2006); (2) measurement of wavelength-dependent eclipse timing in interacting binaries where mass transfer produces chromatic effects; and (3) calibration of photometric timing systematics in large time-domain surveys such as the Vera C. Rubin Observatory Legacy Survey of Space and Time (LSST).

Table 4. Comparison of Vacuum Dispersion Constraints

Method / Reference	Source Class	Wavelength / Energy	Baseline	$\|\Delta c/c\|$ Limit	Notes
V. Vasileiou et al. (2013)	GRBs (combined)	$\sim$0.1–30 GeV	$z \sim 0.1$–4	$\lesssim 10^{-20}$	Fermi-LAT, $n = 1$ LIV
A. A. Abdo et al. (2009)	GRB 090510	31 GeV (single γ)	$z = 0.9$	$\lesssim 2 \times 10^{-18}$	Single photon limit
B. E. Schaefer (1999)	GRBs (4 events)	$\sim$0.03–2 MeV	$z \sim 0.2$–2	$\lesssim 10^{-17}$	BATSE time lags
J. Ellis et al. (2006)	GRBs	MeV–GeV	$z \lesssim 6$	$\lesssim 10^{-17}$	Spectral-lag analysis
J.-J. Wei et al. (2015)	FRBs	$\sim$1 GHz (radio)	cosmological	—	DM-subtracted; plasma foreground
B. Warner & R. E. Nather (1969)	Crab pulsar	0.54 μm–1.2 m	2 kpc	$< 4 \times 10^{-7}$	Optical-to-radio comparison
This work	Eclipsing binaries	440–800 nm (optical)	28–1639 pc	$< 3.75 \times 10^{-10}$	FC 95% CL, B–I band

NOTE—All limits are approximate and expressed as $|\Delta c/c|$ for direct comparison. Gamma-ray limits are converted from $E_{\rm LIV}$ assuming the characteristic photon energy of each analysis. The Warner & Nather limit spans optical-to-radio wavelengths; our result is the first purely optical constraint. See Figure 5 for a graphical comparison.

5.6. *Future Improvements*

The measurement presented here is firmly statistics-limited, with systematic uncertainties contributing only 2.0% of the total variance (Table 3). This implies that the sensitivity of the method can be improved substantially through several avenues:

More targets at greater distances. The constraint scales linearly with the maximum distance in the sample. Our most distant target, AW Peg at 1639 pc, already provides the dominant distance leverage. Extending the sample to targets at 5–10 kpc—accessible with 2–4 m class telescopes—would improve the constraint by a factor of 3–6. Southern-hemisphere targets would roughly double the available sample.

Improved timing precision. The per-target timing uncertainty is currently 12–36 s (Table 2), dominated by photon noise and red noise from a 0.5 m aperture. A 2 m telescope would reduce photon noise by a factor of $\sim$4, and multi-epoch averaging (enabled by the repeatability of eclipses) would reduce statistical uncertainties as $1/\sqrt{N_{\rm epochs}}$.

Space-based photometry. Data from *TESS* and *Kepler/K2* provide continuous, red-noise-free light curves of eclipsing binaries, though the broadband filters of these missions limit the chromatic timing analysis. Combining space-based geometric constraints with ground-based multi-band timing would reduce degeneracies in the eclipse model.

Narrowband filters. Replacing the broad Johnson–Cousins filters with narrowband interference filters would provide finer spectral resolution, enabling constraints on the shape of the dispersion relation across the optical window rather than a single B–I measurement.

6. CONCLUSIONS

We have presented the first test of vacuum dispersion using eclipsing binary timing at optical wavelengths. By measuring the inter-band timing offset $\Delta T_0(B,I) = T_0(B) - T_0(I)$ for five Algol-type eclipsing binaries spanning distances of 28–1639 pc and applying a chromatic correction based on stellar limb-darkening models, we have isolated the timing residual attributable to a frequency-dependent speed of light and tested it for the distance-dependent signature predicted by vacuum dispersion.

The Feldman–Cousins 95% confidence level upper limit on the fractional vacuum dispersion between the B (440 nm) and I (800 nm) bands is $|\Delta c/c| < 3.75 \times 10^{-10}$. This result is supported by strong Bayesian evidence for the null hypothesis ($\ln B_{01} = 5.81$) and is robust to the choice of regression methodology (Bayesian and frequentist estimates agree within 0.00σ) and to the removal of any single target from the sample (jackknife ratio 2.87 < 3).

The chromatic correction methodology we have developed enables the reliable separation of astrophysical (limb-darkening) and potential dispersive contributions to the inter-band timing offset. The approach is general and can be applied to any multi-band timing study of eclipsing binaries or transiting exoplanets.

While this constraint is not competitive with gamma-ray tests of Lorentz invariance violation within the standard E^n power-law parametrization—the Fermi-LAT limit is approximately eight orders of magnitude more constraining at GeV energies—the present measurement fills a gap in the multi-wavelength coverage of vacuum dispersion constraints. It represents, to our knowledge, the first purely optical-band measurement, improving upon the optical-to-radio result of B. Warner & R. E. Nather (1969) by a factor of $\sim$1066 at optical wavelengths alone. The measurement is statistics-limited, with clear pathways to improvement through larger telescopes, more distant targets, and multi-epoch averaging.

ACKNOWLEDGMENTS

Facilities: PlaneWave CDK 0.5m

Software: `ellc` (P. F. L. Maxted 2016), `emcee` (D. Foreman-Mackey et al. 2013), `dynesty` (J. S. Speagle 2020), `astropy` (Astropy Collaboration et al. 2022), `ccdproc` (M. Craig et al. 2017), `photutils` (L. Bradley et al. 2022), `matplotlib` (J. D. Hunter 2007)

REFERENCES

Abdo, A. A., Ackermann, M., Arimoto, M., et al. 2009, Nature, 462, 331, doi: 10.1038/nature08574

Akritas, M. G., & Bershady, M. A. 1996, The Astrophysical Journal, 470, 706, doi: 10.1086/177901

Amelino-Camelia, G. 2013, Living Reviews in Relativity, 16, 5, doi: 10.12942/lrr-2013-5

Astropy Collaboration, Price-Whelan, A. M., Lim, P. L., et al. 2022, The Astrophysical Journal, 935, 167, doi: 10.3847/1538-4357/ac7c74

Bay, Z., & White, J. A. 1972, Physical Review D, 5, 796, doi: 10.1103/PhysRevD.5.796

Bradley, L., Sipőcz, B., Robitaille, T., et al. 2022, photutils: Background and source extraction tools, Zenodo, doi: 10.5281/zenodo.6825092

Brecher, K. 1977, Physical Review Letters, 39, 1051, doi: 10.1103/PhysRevLett.39.1051

Claret, A., & Bloemen, S. 2011, Astronomy & Astrophysics, 529, A75, doi: 10.1051/0004-6361/201116451

Colladay, D., & Kostelecký, V. A. 1998, Physical Review D, 58, 116002, doi: 10.1103/PhysRevD.58.116002

Craig, M., Crawford, S., Deil, C., et al. 2017, ccdproc: CCD data reduction, Zenodo, doi: 10.5281/zenodo.1069648

de Sitter, W. 1913, Physikalische Zeitschrift, 14, 429

Eastman, J., Siverd, R., & Gaudi, B. S. 2010, Publications of the Astronomical Society of the Pacific, 122, 935, doi: 10.1086/655938

Ellis, J., Mavromatos, N. E., Nanopoulos, D. V., Sakharov, A. S., & Sarkisyan, E. K. G. 2006, Astroparticle Physics, 25, 402, doi: 10.1016/j.astropartphys.2006.04.001

Feldman, G. J., & Cousins, R. D. 1998, Physical Review D, 57, 3873, doi: 10.1103/PhysRevD.57.3873

Foreman-Mackey, D., Hogg, D. W., Lang, D., & Goodman, J. 2013, Publications of the Astronomical Society of the Pacific, 125, 306, doi: 10.1086/670067

Hunter, J. D. 2007, Computing in Science & Engineering, 9, 90, doi: 10.1109/MCSE.2007.55

Kelly, B. C. 2007, The Astrophysical Journal, 665, 1489, doi: 10.1086/519947

Kipping, D. M. 2013, Monthly Notices of the Royal Astronomical Society, 435, 2152, doi: 10.1093/mnras/stt1435

Mattingly, D. 2005, Living Reviews in Relativity, 8, 5, doi: 10.12942/lrr-2005-5

Maxted, P. F. L. 2016, Astronomy & Astrophysics, 591, A111, doi: 10.1051/0004-6361/201628579

Pont, F., Zucker, S., & Queloz, D. 2006, Monthly Notices of the Royal Astronomical Society, 373, 231, doi: 10.1111/j.1365-2966.2006.11012.x

Schaefer, B. E. 1999, Physical Review Letters, 82, 4964, doi: 10.1103/PhysRevLett.82.4964

Speagle, J. S. 2020, Monthly Notices of the Royal Astronomical Society, 493, 3132, doi: 10.1093/mnras/staa278

Vasileiou, V., Jacholkowska, A., Piron, F., et al. 2013, Physical Review D, 87, 122001, doi: 10.1103/PhysRevD.87.122001

Warner, B., & Nather, R. E. 1969, Nature, 222, 157, doi: 10.1038/222157a0

Wei, J.-J., Gao, H., Wu, X.-F., & Mészáros, P. 2015, Physical Review Letters, 115, 261101, doi: 10.1103/PhysRevLett.115.261101